

## Article

# Effect of Serpentine Flow Field Channel Dimensions and Electrode Intrusion on Flow Hydrodynamics in an All-Iron Redox Flow Battery

Rakesh Basavegowda Krishnappa <sup>1</sup>, S. Gowreesh Subramanya <sup>2</sup>, Abhijit Deshpande <sup>3</sup>  
and Bharatesh Chakravarthi <sup>4,\*</sup>

<sup>1</sup> Department of Mechanical Engineering, Jyothy Institute of Technology, Bengaluru 560052, Karnataka, India

<sup>2</sup> Department of Mechanical Engineering, JSS Academy of Technical Education, Bengaluru 560059, Karnataka, India

<sup>3</sup> Domain Expert, Powertrain CFD, Mercedes-Benz RD, Bengaluru 560066, Karnataka, India

<sup>4</sup> School of Computing and Augmented Intelligence, Arizona State University, Tempe, AZ 85287, USA

\* Correspondence: bshettah@asu.edu; Tel.: +1-602-716-1642

**Abstract:** This paper presents a study on flow hydrodynamics for single-channel serpentine flow field (SCSFF) and cross-split serpentine flow field configurations (CSSFF) for different geometric dimensions of channel and rib width ratios with electrode intrusion over varying compression ratios (CRs) in an all-iron redox flow battery. Pressure drops ( $\Delta p$ ) measured experimentally across a cell active area of 131 cm<sup>2</sup> for different electrolyte flow rates were numerically validated. A computational fluid dynamics study was conducted for detailed flow analyses, velocity magnitude contours, flow distribution, and uniformity index for the intrusion effect of a graphite felt electrode bearing a thickness of 6 mm with a channel compressed to varying percentages of 50%, 60%, and 70%. Experimental pressure drops ( $\Delta p$ ) over the numerical value resulted in the maximum error approximated to 4%, showing good agreement. It was also reported that the modified version of the cross-split serpentine flow field, model D, had the lowest pressure drop,  $\Delta p$ , of 2223.4 pa, with a maximum uniformity index at the electrode midplane of 0.827 for CR 50%, across the active cell area. The pressure drop ( $\Delta p$ ) was predominantly higher for increased compression ratios, wherein intrusion phenomena led to changes in electrochemical activity; it was found that the velocity distribution was quite uniform for a volumetric uniformity index greater than 80% in the felt.

**Keywords:** iron redox flow battery; serpentine flow field; flow hydrodynamics; computational fluid dynamics; intrusion phenomenon; graphite felt electrode; uniformity index



**Citation:** Krishnappa, R.B.; Subramanya, S.G.; Deshpande, A.; Chakravarthi, B. Effect of Serpentine Flow Field Channel Dimensions and Electrode Intrusion on Flow Hydrodynamics in an All-Iron Redox Flow Battery. *Fluids* **2023**, *8*, 237. <https://doi.org/10.3390/fluids8080237>

Academic Editors: Nilanjan Chakraborty, Leonardo Di G. Sigalotti and Carlos Enrique Alvarado-Rodríguez

Received: 10 June 2023

Revised: 7 August 2023

Accepted: 8 August 2023

Published: 21 August 2023



**Copyright:** © 2023 by the authors. Licensee MDPI, Basel, Switzerland. This article is an open access article distributed under the terms and conditions of the Creative Commons Attribution (CC BY) license (<https://creativecommons.org/licenses/by/4.0/>).

## 1. Introduction

The current annual global energy generation capacity is estimated to be more than 20 TW (terawatt), and the energy consumption is estimated to be more than 15 TW. The major portion of contemporary energy needs is fulfilled by conventional energy sources, i.e., fossil fuels such as coal, natural gas, oil, etc., whereas the rate of energy consumption is increasing exponentially, and if it continues to grow at this pace, the predicted energy needs might double by 2050. Hence, there is a peak in demand for energy production, storage, and distribution. Environmental concerns over the use of non-renewable energy and their resource constraints, combined with energy security concerns, represent a launching pad to generate high-grade energy, i.e., electricity obtained from renewable energy sources. The energy obtained from solar power and wind, being intermittent in nature, poses a tough challenge for grid operators to store and retrieve. One such technology, which is ideal and also sustainable, is electrical energy storage systems (ESSs), which is considered to be a key enabler of smart grids or future grids. This technology might smoothen out the variable nature of renewable energy production and distribution, act as a bi-directional power

regulator, offset the surplus of generated energy for future needs, facilitate effective energy storage, delivery, ensure improved grid reliability and utilization, and hence, represents a stable candidate for future electric grids. Many such energy storage technologies, such as mechanical, electrochemical (batteries), thermal, electrical, and hydrogen storage systems, already exist in the commercial domain. However, substantial research and development still needs to be conducted in the fields of material and technological advances to enhance electricity distribution, power backup range, duration of storage, and energy scale-up. These storage technologies are limited on the system-level usage suitability for required applications [1–4].

Research on electrochemical energy storage systems has been steadily growing since the flow battery concept evolved approximately four decades ago, and it is a promising agent for medium to large kilowatt-scale energy storage applications [5–7]. Redox flow battery (RFB) technology is well established and is gaining traction due to its suitable integration to achieve efficiency, scalability, rapid sensitivity, longer life cycle, less maintenance, low cost, flexibility in energy and power capacity, the least impact on environment, and as one of the many electrochemical energy storage (ESS) methods, particularly to store renewable energy. RFBs are the best alternative to Li-ion stationary systems and have been authenticated and standardized by the International Electrochemical Commission as grid storage systems [8,9].

RFBs represent many forms, developed as aqueous nature, based on their redox couples, including iron–chromium, bromine–polysulfide, quinone–bromine, zinc–bromine, and all-vanadium RFBs; single-metal-based, including all-iron, all-lead, and all-copper RFB systems; and non-aqueous forms, including all-uranium and all-neptunium RFBs dissolved in non-aqueous solvents. Vanadium-based batteries are well-established and commercially adopted flow batteries; however, they have certain operational limitations due to the inherent cross-contamination problem caused by the diffusion of different redox ions across the membrane, and low solubility [10,11].

We shifted our interest towards the initially developed iron-based RFBs: iron–chromium, iron–cadmium, zinc–iron, and iron–vanadium; these batteries are best suited for certain system-based applications. They persist with certain difficulties in improving system efficiency due to the inherent nature of redox couple activity of slow kinetic reactions, poor reversibility, and hydrogen evolution (side reaction). Cross-contamination results in self-discharge and a high operating temperature. Some oxidation forms are toxic in nature. Low solubility (limiting the energy density) and precipitation issues at about a 40 °C operating temperature lower the electrolyte utilization by blocking the effect due to electrodeposition, which essentially limits the energy capacity during charging. Dendrite formation can lead to short circuits and a high cost of vanadium-based species. Certain beneficial features of all-iron RFBs have emerged, including a high level of solubility, improved discharge energy density, operation stability with less precipitation even at increased electrolyte temperatures, non-toxic, environmentally friendly, low-cost redox species, and abundant earth metal [12,13]. The energy/power density of all-iron RFBs is reasonably high, with the least capital cost. To achieve this, a specific selection of key materials such as electrodes, electrolytes, and ion exchange membranes, in addition to an optimized flow field configuration, are the key components.

In an RFB, the positive and negative species of electrolyte are circulated through the cell stack, where charge and discharge take place before being returned to the external storage tank. The amount of energy stored depends on the volume of electrolytes, while the peak power density depends on the number and size of the cell stack, wherein both the power and energy stored can be widely varied independently. This feature indeed promotes RFBs as a very attractive alternative for kilowatt-scale energy storage applications [14].

Improvements in power density make RFBs a more competitive option for kilowatt-scale energy storage. The operating power density of an RFB is a function of the rate of electrochemical ionic activity at the electrode felt–electrolyte interface.

Inadequate electrolyte circulation limits the electrocatalytic activity, even though the proper selection of materials and porous media is realized.

The literature reports that the different channel and rib dimensions of a serpentine flow field should be clearly understood for their geometric dimensions, stability, and suitability over a selected cell size, on channel geometry, with dimensions varying about 1 to 2 mm in channel width and rib width occupying between 40% and 50% of the total cell area. The variation in channel dimension is reflected in larger cell sizes with a noticeable change in pressure drop, peak power density, and discharge energy density, thus recommending larger channels with reduced rib width to improve the overall performance of the cell [14,15]. In redox flow battery applications, the electrolyte is a liquid component that flows through a hydraulic diameter of the channel, whereas the results of pressure drop and flow distribution were also dependent on varied rib-to-channel width ratios, increased flow rate, flow circulation, length of flow path, and compression of the porous medium as additional parameters. Recent research and development has been performed to understand the flow hydrodynamics, flow channel interactions (interdigitated, spiral, and serpentine), electrodes, modified forms, and their properties, such as permeability, as a function of compression factors (intrusion effect), on overall battery performance [16–25].

Inherent properties such as permeability, porosity, and pore size of the electrode felt determine the level of diffusion and the drop-in pressure to be incurred for a given electrolyte discharge. Pressure drops ( $\Delta p$ ) between adjacent serpentine flow channels possibly develop convective diffusion in the porous electrode, whereas the flow field (interdigitated) enables the electrolyte to flow along a defined path including the electrode. The increased pressure drop may lead to inadequate electrolyte distribution, resulting in decreased electrocatalytic activity at the electrode–electrolyte interface [26–28].

In addition, the cell-stack design parameters, such as torque applied to hold the cell assembly together to stop leaks, reduce stacking pressure, and decrease electrode compression, effectively determine the permeability. Hydrodynamic interactions are an active function of the cell size, design, and electrolyte circulation rate. One literature review identified a new flow field design, i.e., plug flow, later optimized to a short flow path to regulate the mass transport polarization behavior, which improves performance in redox flow battery systems [29–32].

A few studies have reported that the channel dimensions and electrode intrusion in interdigitated and conventional serpentine flow fields also lead to a pressure drop across the cell stack; their findings were based on understanding the hydrodynamics of the flow along with electrochemical performance studies on vanadium-based battery systems. Analysis of new flow field configurations, electrolyte flow dynamics in adjacent channel dimensions and under rib convection, and pressure drop parameters were addressed. Several significant studies have demonstrated that the serpentine flow channel configuration shows the highest energy efficiency with the least pressure drop, at different operating conditions, and predominantly enhances electrochemical activity in the flow cell battery application [33–36].

The development of a suitable flow field design can certainly reduce the cost of a redox flow battery. Starting from the interdigitate flow field design analysis, the channel and rib dimensions varied to investigate the impact on pressure drop, channel flow volume, flow uniformity, and parameters operating at different current densities. Design optimization is one component that can reduce the overall setup cost of the cell stack and also increase system performance.

Electrolyte flow distribution is an important factor that contributes to the performance of a redox flow battery, wherein the interdigitated and serpentine flow fields are simulated and studied closely for pressure drop parameters and computational fluid dynamics; the study revealed ‘under the rib convection’ for both flow field designs, but with a shorter residing time for the interdigitated flow field, showing superior electrochemical performance. The literatures quantify the simulation results of interdigitated and serpentine flow fields with details of channel passage and the dependence of pressure loss on cell

size and flow field design, giving an understanding of the slow flow regions of mass transport behavior and the electrode parameters, which influence pressure drops. The most cost-effective way to build a redox flow battery is by optimizing flow field design, which leads to reduced stack area and increased power density [37–40].

The most significant way to recognize the influence of flow circulation and uniform distribution over the entire cell area for effective ionic activity is through design parameter changes such as charge and discharge energy capacity, peak power, and energy efficiency, which also depend on the stack size and electrolyte volume discharge. Furthermore, the main scope of this study focused on optimizing a modified version of serpentine flow field configurations at varying electrolyte flow rates to predominantly showcase the enhanced flow distribution and uniformity at the lowest possible pressure drop across the cell, and ultimately increase the electrochemical performance.

This paper reports an experimental study on pressure drop parameters for single and cross-split serpentine flow field configurations with the electrode intrusion effect as a function of the compression ratio at varying flow rates, with numerical validation. The flow hydrodynamic study was carried out using computational fluid dynamics (CFD) on modified versions of the cross-split serpentine flow field for different channel dimensions (rib-to-channel width ratios) with suitable porous media (graphite felt electrode) subjected to different compression ratios at varying electrolyte flow rates to analyze parameters such as pressure drop across the active cell area, velocity magnitude contours, flow circulation, and uniform distribution. The electrode–felt permeability values were obtained using a Tamayol–Bahrami correlation model [41]. The most suitable model for the electrode’s planar fibrous microstructure was in close agreement with the rayon-based graphite felt material chosen in this study. Details of these studies and the results obtained are discussed below.

## 2. Materials and Methods

The systematic assembly of an all-iron redox flow battery (AIRFB) cell is depicted in Figure 1. The main components of AIRFB cells are graphite plates with flow channels, electrodes, anionic membrane, ferrous solution as an electrolyte, copper current collectors, gaskets, and end plates.

The chemical reactions in the battery are given by Equations (1)–(3) [37]

Positive electrode:



Negative electrode:



Overall:



The AIRFB system has optimal power density and current capacity, whereas the stack is a single-cell assembly. During the operation, an electrolyte is constantly circulated using a peristaltic pump through the graphite plate flow channel from the respective electrolyte storage tank. The performance of the system was evaluated based on the columbic, voltaic, and energy efficiencies, energy density, and depth of discharge.

The models developed for this study had the same active cell area, 131 cm<sup>2</sup>, with fixed inlet and outlet positions. Electrode graphite felt, a porous medium with a thickness of 6 mm, was specifically selected based on certain criteria such as electrical conductivity, surface area, pore size, pretreatment (thermal treatment), and electrochemical activity (cell resistance and cell efficiency). An electrolyte solution containing ferrous chloride tetrahydrate (FeCl<sub>2</sub>) was proportionately mixed with 2 moles of ammonium (NH<sub>4</sub>), 3.25 moles of chloride (Cl<sub>2</sub>), and 0.3 moles of ascorbic acid (C<sub>6</sub>H<sub>8</sub>O<sub>6</sub>) to maintain ideal pH conditions [37].

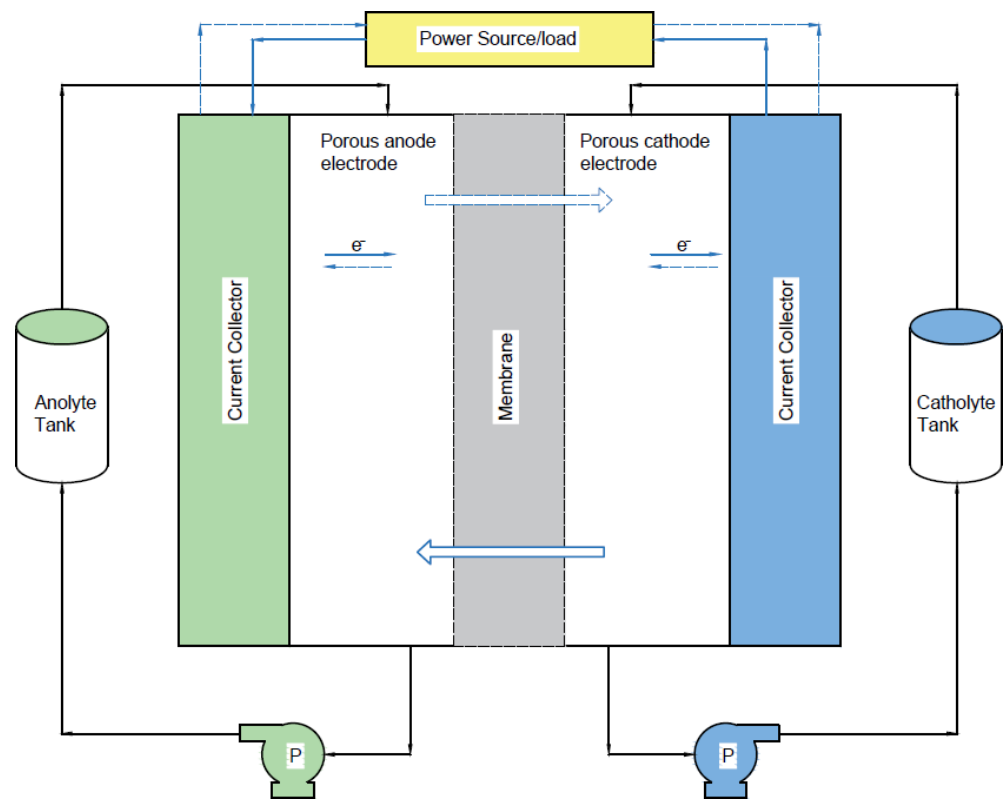


**Figure 1.** A Systematic Assembly of an All Iron Redox Flow Battery.

2.1. Flow Field without Felt Model

Details of the A, B, C, and D flow field models of cross-split serpentine flow field configurations with varying geometrical dimensions are presented in Table 1. These models were designed using SolidWorks Premium 2018 SP 4.0, developed by Dassault Systems. Models with graphite plates of 10 mm thickness, ET-10 (isostatic nature) grade, with the highest thermal conductivity had the lowest ash content compared with other commercially available grades, such as T-2, T-8, and EX-70.

**Table 1.** Geometric Parameters of the Flow Field Configurations.

Models	Width (mm)		Channel Depth (mm)	No of Channels		No. of Bends (N <sub>b</sub> )	Total Flow Path Length (mm)	Active Area (mm <sup>2</sup> )	Channel Hydraulic Diameter (mm)
	Channel	Rib		Horizontal	Vertical				
A	2	2	2	17	24	40	3037		2
B	2	2	3	17	24	40	3037		2.4
C	3	3	2	13	19	31	2364		2.4
D	3	3	3	13	19	31	2364	13,095	3

The graphite plates were subjected to CNC milling operations to generate engraved channels of the required dimensions, as shown in the CAD model depicted in Figure 2 for a precision flow path to ensure the uniform flow circulation of electrolyte solution over the entire cell active area to enhance the electro-kinetic activity at the electrode–electrolyte interface. The graphite plate used in the milling operation was purchased from IndianTech, Bengaluru, India.

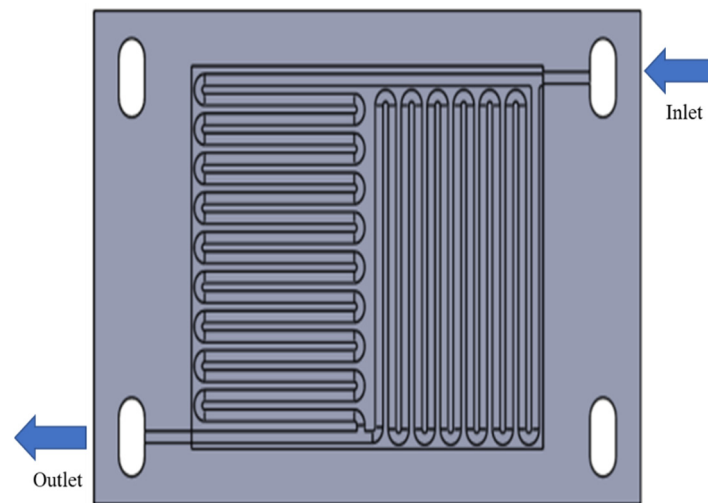


**Figure 2.** The  $3 \times 3$  Cross Split Serpentine Flow Field Model (CSSFF).

### 2.2. Flow Field with Felt Model

The flow field integrated with graphite porous electrode felt with an original thickness ( $t$ ) of 6 mm is shown in Figure 3. The graphite felt electrodes were purchased from Rayon Graphite Felt (AGFHT), USA. The anionic membrane (FUMASEP FAP-375PP) model and Nafion binder used therein were obtained from Fuel Cell Store, USA. The other essential battery components, such as epoxy endplates of 15 mm thickness, copper plates, and gaskets, were fabricated in-house for our investigation.

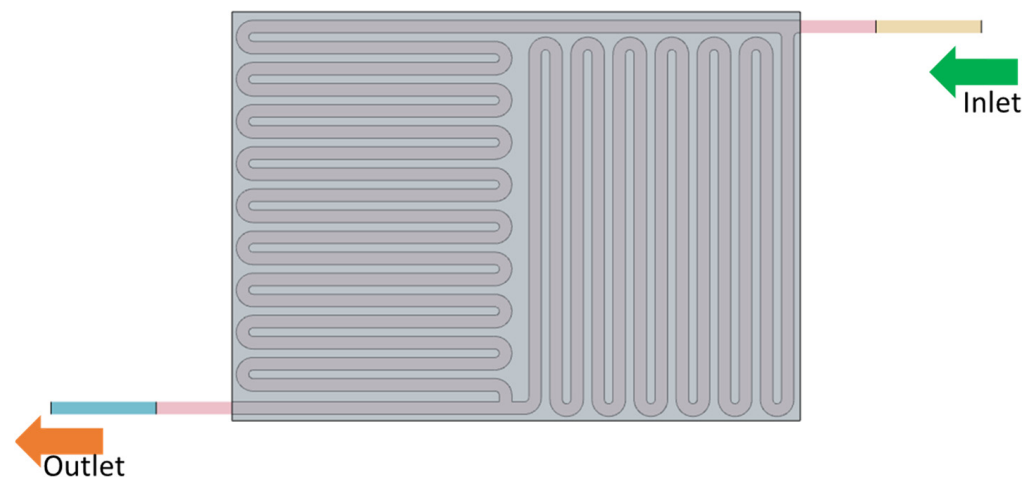


**Figure 3.** The  $3 \times 3$  cross-split serpentine flow field with graphite felt model (CSSFF).

The flow characteristic analyses were carried out considering the felt channel intrusion factor at different compression ratios over the varying channel-rib geometric dimensions detailed in Table 1. Apart from the pressure drop effect caused by the non-uniformity of electrolyte flow circulation, the intrusion effect does play a vital role in the uniform distribution rate over the entire cell area. Establishing the highest ionic conductivity reaction rate for minimum electrode channel intrusion at different compression ratios resulted in a significant change in the pressure gradient over the entire active cell area, as reported by the measurements and CFD analysis [20]. A few studies have recommended an ideal electrode thickness for enhanced electrochemical performance [22]; however, a higher percentage of electrode compression will result in decreased porosity, which, in turn, decreases the rate of electrolyte circulation through the electrode and under the rib convection, thereby reducing the mass transport polarization [39].

### 2.3. Circuit Analogy Model

A hydraulic circuit model concept was developed corresponding to the flow field CAD model, to better analyze the electrolyte flow characteristics and resistance offered, as shown in Figure 4. Here,  $\dot{m}$  represents the electrolyte mass flow rate;  $\dot{m}_1$  and  $\dot{m}_2$  are split mass flow, i.e., correlating to vertical and horizontal channels of the model, respectively; and  $R_1$  and  $R_2$  are resistance values corresponding to the vertical and horizontal halves of the model, respectively. Henceforth, the analysis considered the mass flow to be equivalent to the current flow, and the resistance was equivalent to flow deceleration due to skin friction and bend losses in the passage.

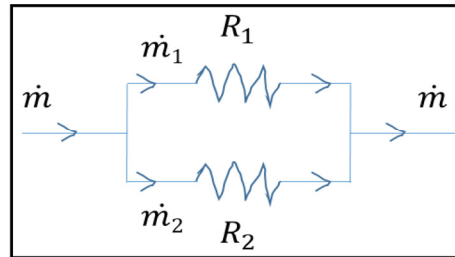


Figure 4. Cross Split Serpentine Flow Field (CSSFF) Circuit Analogy Model.

The assumptions made for the selected model were that the flow analysis was steady, laminar, incompressible in nature, and isothermal.

Pressure drops for cross-serpentine channel [14] are given by:

$$\Delta p = 0.5\rho u^2[4fL/D + N_bK_b] \tag{4}$$

where  $u$  is the average flow velocity,  $L$  is the straightened length along the channel path,  $D$  is the hydraulic diameter,  $f$  is the Fanning friction factor,  $N_b$  is the number of bends, and  $K_b$  is the bend loss coefficient.

The momentum conservation equation for flow through the porous substrate is given by:

$$\rho \frac{du}{dt} = \rho g - \frac{\partial p}{\partial x} + \mu \nabla^2 u + S_m \tag{5}$$

$$S_m = \Delta p/L = \alpha V + \beta V^2 \tag{6}$$

where  $\alpha$  is the viscosity coefficient and  $\beta$  is the inertial resistance coefficient. Pressure drops in the porous substrate were determined using the source term Equation (6).

The source term was added to the momentum equation to account for viscous and inertial effects. Compression ratio and permeability equations are referenced from [25].

The compression ratio (CR) under the rib and channel is calculated by the equation:

$$CR_{rb} = 1 - \frac{t_c}{t} \tag{7a}$$

$$CR_{ch} = 1 - \frac{t_c + d}{t} \tag{7b}$$

where  $t$ ,  $t_c$ , and  $d_{fi}$  are the original felt thickness, compressed felt thickness, and depth length of felt intrusion into the channel, respectively.

Similarly, permeability ( $K$ ) was calculated corresponding to the compression ratio using the following equation from the Tamayol–Bahrami model [41]

$$k/d^2 = 0.012(1 - \phi) [\pi/4\phi^2 - 2(\pi/4\phi) + 1] [1 + 0.72\phi/(0.89 - \phi)^{0.54}] \tag{8}$$

where  $\phi = (1 - \epsilon)$ ,  $\epsilon$  is the porosity,  $K$  is the permeability,  $d$  is the fiber diameter, and  $\phi$  is the solid volume fraction.

The volume uniformity index is as shown below. [37]

$$\phi = 1 - \frac{\sum c[v_c - v]}{V_c / 2[v] \sum c V_c} \quad (9)$$

### 3. Experimental Study

Experimental investigation of a single-channel serpentine flow field (SCSFF), with an active cell area of  $131 \text{ cm}^2$ , i.e.,  $135 \text{ mm length} \times 97 \text{ mm width}$ , wherein 17 parallel channels are aligned along the longer length of the rectangular cell. Notably, all are square channels with a  $2 \text{ mm}$  hydraulic diameter, each placed at an equal distance, as depicted in Figure 5. Geometrical details of the flow field along with the felt are as follows: channel width of  $2 \text{ mm}$ , rib width of  $2 \text{ mm}$ , channel depth of  $2 \text{ mm}$ , and Rayon-based graphite felt electrode (AGFHT) with a thickness of  $6 \text{ mm}$  and subjected to electrode compression (change in original thickness) to  $60\%$  and graphite plate (isostatic grade) with a thickness of  $10 \text{ mm}$ .

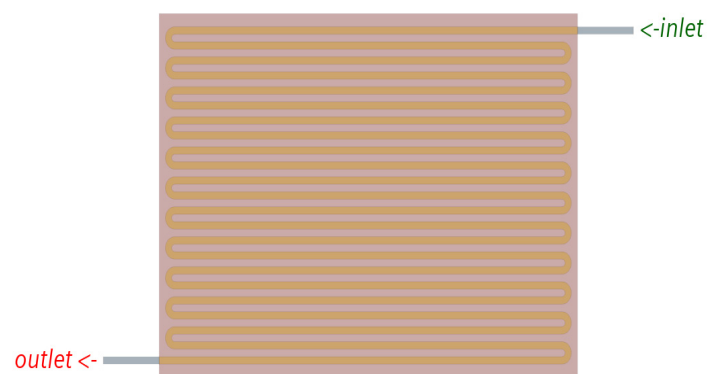


**Figure 5.** The  $2 \times 2$  single-channel serpentine flow field with electrode felt (SCSFF) CFD flow field model.

The fabricated setup consisting of end plates on either side connected to electrolyte flow pipes on the top left and bottom right corners, representing entry and exit passages for electrolyte flow to separate analytic and catalytic tanks, respectively, is shown in Figure 6a. The pressure gradient across the active cell area was able to be measured using a U-tube manometer, as shown in Figure 6b. The two separate electrolyte tanks on either side were filled to a volume of  $250 \text{ mL}$ . The prepared solution contained iron species  $\text{Fe}^{2+}/\text{Fe}^{3+}$  and  $\text{Fe}^{2+}/\text{Fe}$ , acting as positive and negative electrolytes, respectively, as stated in Equations (1) and (2).

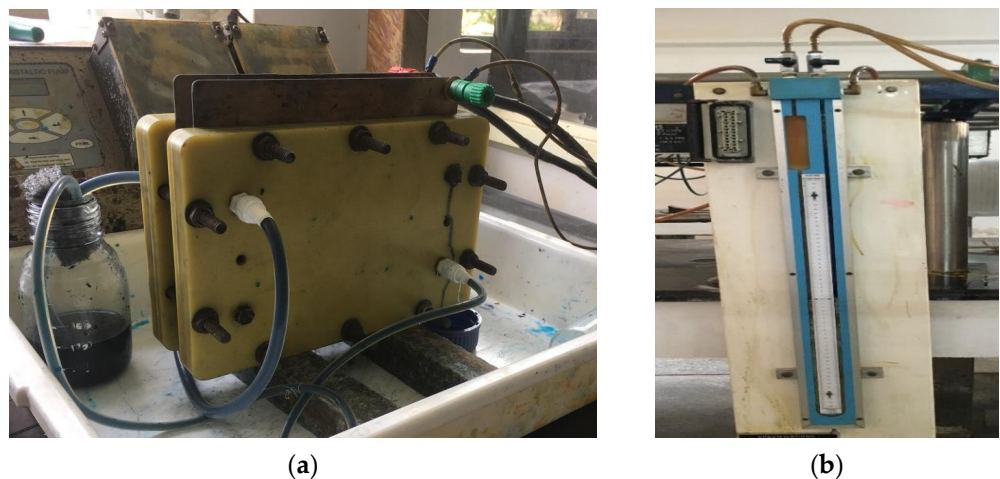


**Figure 6.** (a) An Experimental Set Up of Battery Stack. (b) U Tube Manometer to Measure Pressure Drop.

Experiments were conducted on a single-channel serpentine flow field (SCSFF) with electrode felt intrusion at CR 60% for varying electrolyte flow rates to determine the pressure drop,  $\Delta p$ , data using a U-tube manometer, and were compared with CFD data. The results presented in Table 2 show that the pressure drop values are close and approximate for both cases. The results clearly show that there is still scope for optimization of the flow field to reduce the pressure drop,  $\Delta p$ , to a great extent, improve the flow distribution and uniformity, and further enhance the electrochemical activity at the electrode–electrolyte interface. This eventually encouraged us to redesign and simulate modified versions of the serpentine flow field, as listed in Table 1.

**Table 2.** Comparison of CFD and Experiment pressure drop for  $2 \times 2$  SCSFF.

Boundary Condition	Flow Rate mL/min	Reynold's (Re)	CFD Pressure Drop p [Pa]	Exp Pressure Drop p [Pa]
1	30	180	4898.61	5100.00
2	60	360	11,188.90	11,600.00
3	90	540	17,772.72	18,550.00
4	120	720	24,647.79	25,750.00
5	150	899	31,815.35	33,250.00

#### 4. CFD Analysis

##### 4.1. Flow Field Model Analysis

Cross-split serpentine flow field models with different geometric dimensions were designed and simulated using commercially available software, i.e., Siemens Sim-Center STAR CCM+ tool 15.02.009 R8 (double precision). Simulations carried out using a 3D unstructured mesh polyhedral type with prism cells in the order of 10 million generated for near-wall treatment [37] are depicted in Figure 7. Suitable boundary conditions were applied, with a laminar flow regime, isothermal process, and the electrode felt modeled as porous media to analyze the pressure gradient across the cell, velocity variation at different compression ratios, and electrolyte circulation at varying flow rates, to understand the uniform flow distribution pattern over the entire active cell area on the two half-cell regions, one on the positive half and the other on the negative half, in which each cell was integrated within the electrode and flow field domains. A sample model is depicted in Figure 3.

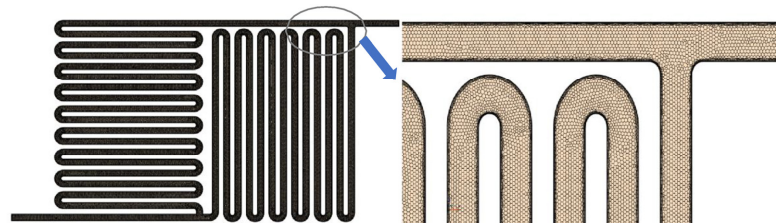


**Figure 7.** Illustration of Cross Split Serpentine Flow Field Polyhedral Mesh.

##### 4.2. Flow Field with the Electrode Intrusion Model

Figure 8 shows the electrode felt intrusion with an uncompressed region into the channel and under-rib compression region, with electrolyte flow rates,  $Q_{ch}$  and  $Q_{pm}$ , flowing through the channel and porous electrode medium. The properties of the selected electrode were a plane permeability of  $1.498 \times 10^{-6} \text{ m}^2$ , porosity of 0.80, and a fiber diameter of 0.0155 mm. The electrolyte had a viscosity of 0.0013897 Pa-s. Electrode intrusion into the channel is a strong function of compression ratios, which reduce the hydraulic diameter of the channel and thereby increase the mean effective flow velocity, resulting in an increased pressure drop. Equation (10) shows the calculation of the intrusion depth in terms of the compression ratio (CR) and the uncompressed thickness of the graphite felt.

$$\frac{d}{[t \cdot (1 - CR)]} = 0.67 - 0.058t (1 - CR) \quad (10)$$

The increase in electrode thickness would increase the pressure drop,  $\Delta p$  [25]. Intrusion depth values were approximately obtained from the above correlation for the study of different flow field geometries with the same materials and compression ratios. Different compression ratios resulted in different intrusion values and electrode compression for the given flow field, Model D, with channel and rib widths of  $3 \times 3$  mm, increasing the compression ratio (CR) from 50% to 70%. The value of intrusion depth also increased, from 1.78 mm to 2.49 mm, as shown in Table 3. Thus, the pressure drop,  $\Delta p$ , tended to significantly increase, but had less influence on electrolyte circulation and distribution across the entire active cell area.

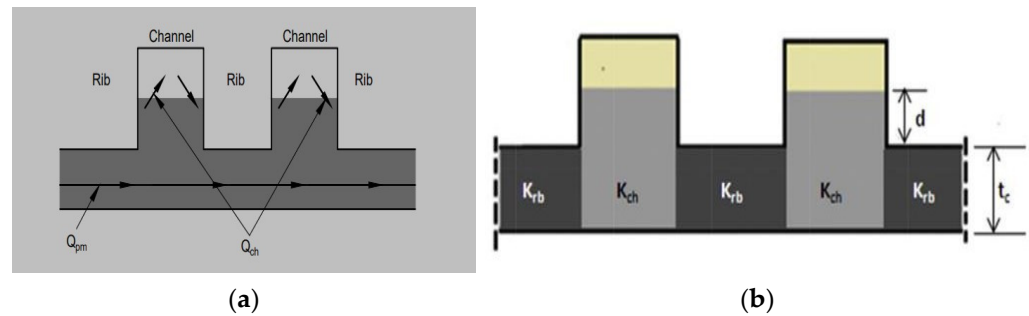


Figure 8. (a) Graphite Electrode Felt Intrusion into Channels. (b) Geometry Modeled for CFD Analysis.

Table 3. Different Compression ratio (CR) corresponding intrusion value for  $3 \times 3$  model.

Case	Graphite Felt Actual Thickness (mm)	CR 50%	CR 60%	CR 70%
Compressed value	6	3	2.4	1.8
Intrusion value		1.78	2.14	2.49

Compression of the porous electrode felt with a thickness of 6 mm into the channel with an electrode intrusion value differed for each compressed case from 50% to 70% of its original thickness, as shown schematically in Figure 9. Model D consisted of flow channels and electrode felt, whereas the reactant activity was higher in the positive electrolyte than in the negative electrolyte [34].

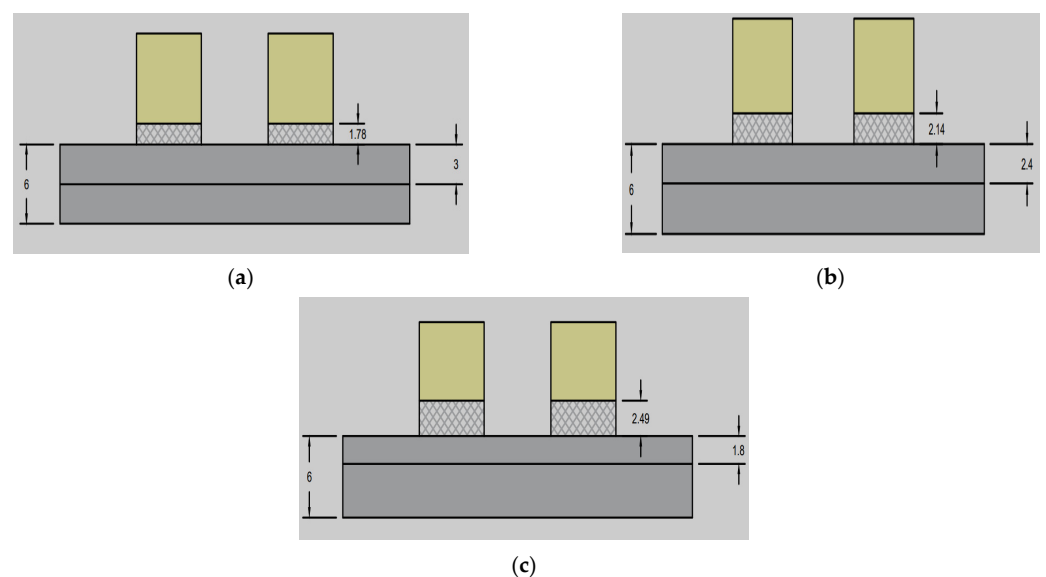
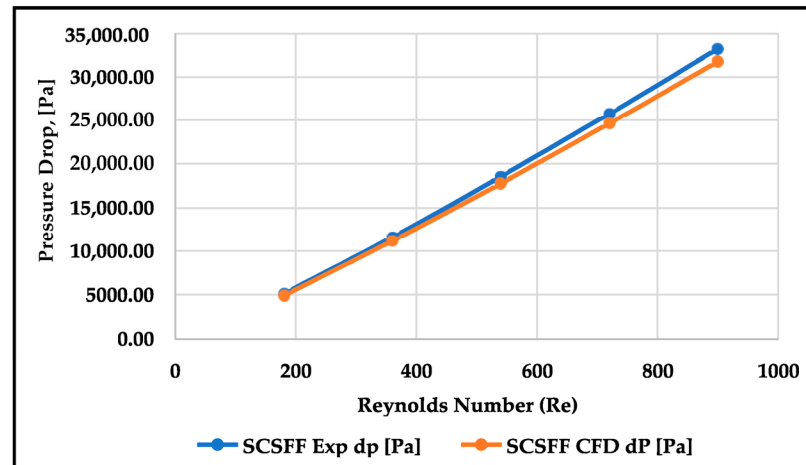


Figure 9. (a–c) are Schematic Representations of the Flow Field with Electrode Felt Intrusion at Varying Compression Ratios (50, 60 and 70%).

## 5. Results and Discussion

### 5.1. Numerical Software Validation

AIRFB (all-iron redox flow battery) systems were constructed using a single-cell active cell area of 131 cm<sup>2</sup>. The experimental results of pressure drop,  $\Delta p$ , obtained for the above cell area were compared with those of numerically analyzed values. The pressure drop curves were derived based on the analysis results of a 2 × 2 single-channel serpentine flow field (SCSFF) with an intrusion effect for varying Reynold’s numbers of 180, 360, 540, 720, and 899 at a 60% compression value, as depicted in Figure 10.



**Figure 10.** Comparison of CFD and Experiment Pressure Drop ( $\Delta p$ ) for the Single Channel Serpentine Flow Field (SCSFF) for Different Reynold’s Number.

To conclude, it was observed that the experimental and numerical results of pressure drop,  $\Delta p$ , were a linear function of Reynold’s number, wherein both the results were in good agreement, as the maximum error is approximately less than 4%.

Figure 11a For the 2 × 2 SCSFF with an electrode intrusion, we observed a gradual decrease in the absolute total pressure from inlet to outlet over the entire active cell area, with the maximum value of 0.31 bar and approximately a 60% compression ratio (CR) for the flow rate of 150 mL/min. Figure 11b,c depict the general velocity magnitude pattern through the channel mid-plane and electrode felt mid-plane; the velocity flow behavior was almost same with the smallest velocity magnitude at the mid portion of the cell and higher velocity magnitude value at inlet and outlet flow regions. Subsequently, newly modeled 3 × 3 cross-split serpentine flow fields were subjected to CFD simulation to understand the better flow hydrodynamics characteristics. Table 4 depicts the experimental and CFD pressure drop values for Model D of the cross-split serpentine flow field (CSSFF).

**Table 4.** Compared experimental and CFD pressure drop values for Model D of the CSSFF at different CRs and for varying flow rates.

Flow Rates mL/min	Compression Ratio %	Experimental CSSFF Pressure Drop, Pa	CFD Model CSSFF Pressure Drop, Pa
30	50.00	1233	1002
	60.00	3128	2789
	70.00	12,450	11,890
90	50.00	1874	1560
	60.00	4840	4150
	70.00	18,300	17,780
150	50.00	2453	2223
	60.00	7350	6941
	70.00	26,130	24,679

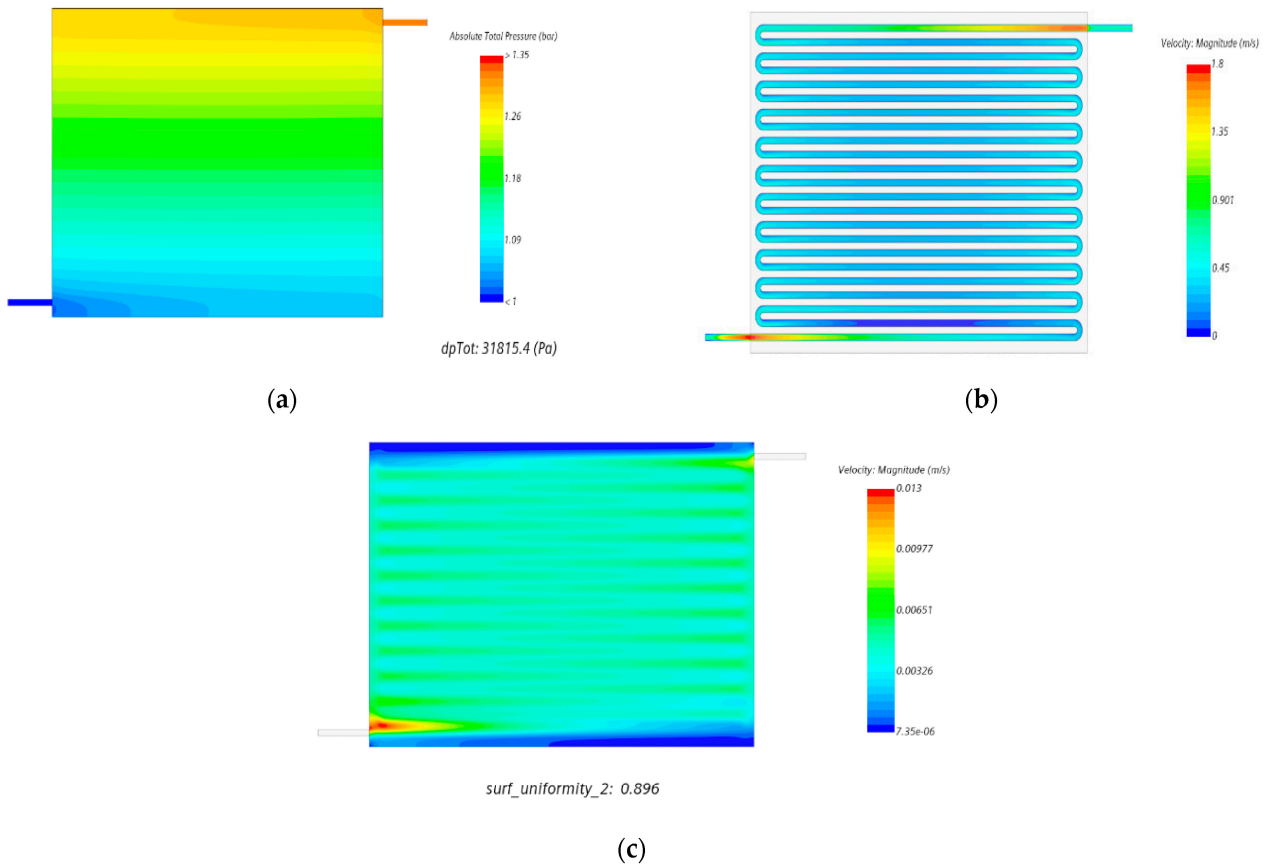


**Figure 11.** (a–c)  $2 \times 2$  single serpentine flow field (SCSFF) absolute total pressure drop with electrode felt intrusion, predicted velocity magnitude at channel mid plane without electrode felt and with electrode felt mid plane 60% CR at 150 mL/min.

In Figure 12, the plotted line graphs represent the variation in pressure drop over an active cell area subjected to different CRs for varying flow rates. Figure 12a–c indicate that the pressure drop varied linearly for 50%, 60%, and 70% CRs, whereas there was a rapid increase in the pressure drop value at 70% CR for all the flow rates. The experimental pressure drop value reached a maximum of 26,130 Pa for the highest flow rate of 150 mL/min. The results demonstrate that linear variation showed good agreement for both the experimental and CFD values, with maximum error approximating 5%.

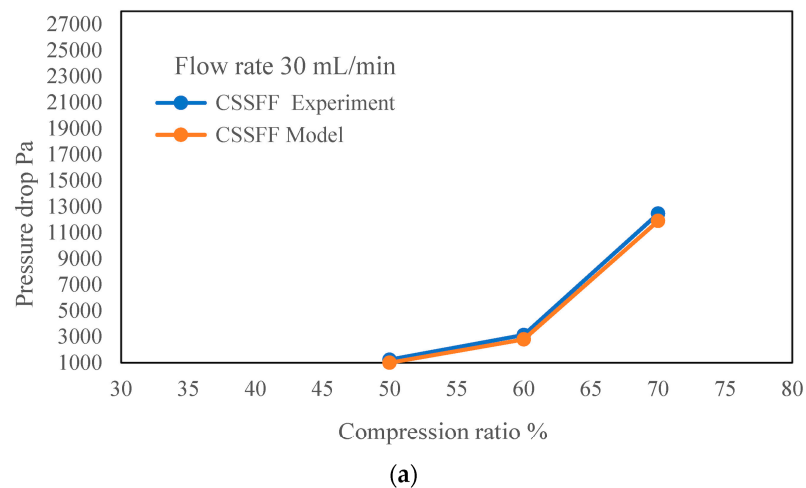
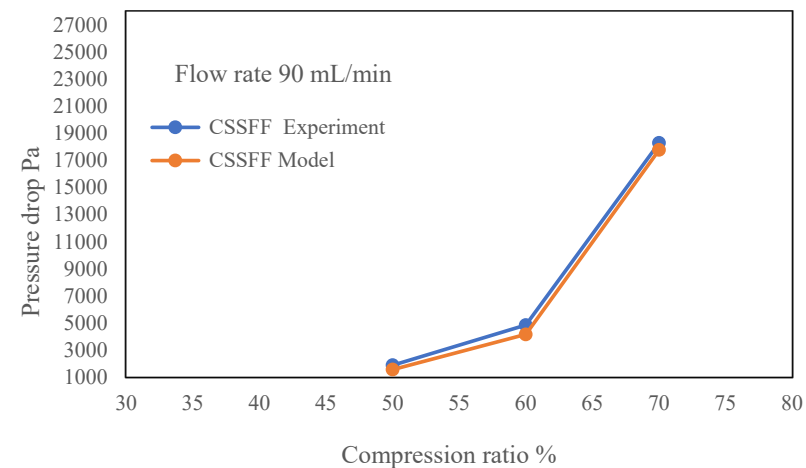
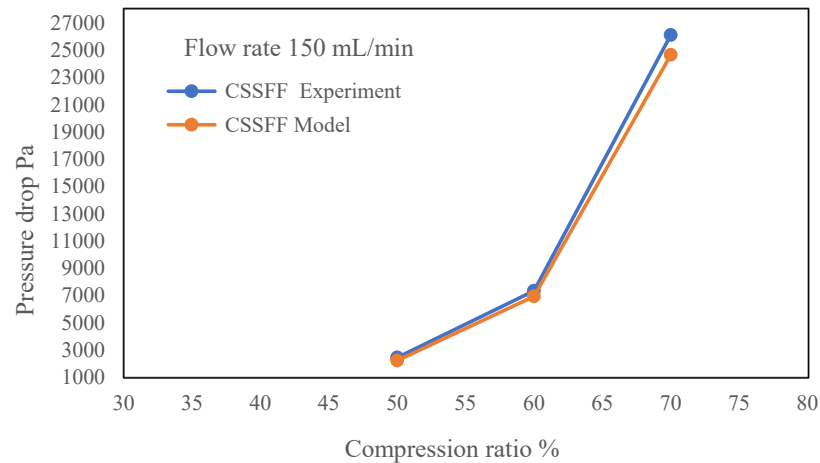


**Figure 12.** Cont.



(b)



(c)

**Figure 12.** (a–c) Comparison of experimental and CFD pressure drop values for model D of CSSFF with an electrode intrusion at CR (50%, 60%, and 70%) for flow rates of 30, 90, and 150 mL/min.

## 5.2. Simulation Results

As observed in Figure 13a–c, the simulated pattern of  $\Delta p$  across the flow domain integrated with the electrode graphite felt with channel intrusion for different compression ratios was at a maximum flow rate of 150 mL/min. The rapid rise in the absolute pressure value was observed more in vertical channels than in horizontal channels, reaching relatively high levels at the right bottom corners and having a lower impact on flow pattern and distribution as the flow is laminar in nature. Meanwhile, the flow was well controlled by a peristaltic pump, which evenly produced pulsatile flow (not linear) in nature and supported the smooth flow and uniform distribution over an entire active cell area, thereby increasing the wettability factor. Hence, the higher the compression ratio, the higher the pressure drop, approximately 3.5 times greater for an individual case at different CRs. The asymmetric flow profiles in Figure 13a–c are due to the effect of the skin friction coefficient and self-weight of the fluid, which are at minimum values over the horizontal channels and slightly higher on the vertical channels represented in color contours.

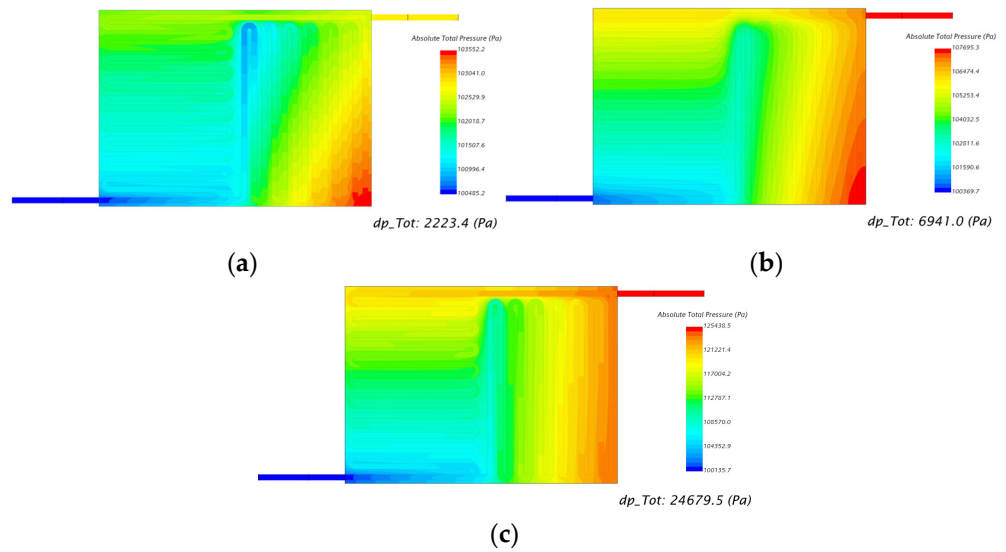


**Figure 13.** Predicted absolute pressure drop for Model D of the CSSFF with an electrode intrusion for a flow rate of 150 mL/min at CRs: (a) 50%; (b) 60%; and (c) 70%.

As observed in Figure 14a–c, the velocity magnitude increased drastically at the channel inlet, split region, and junction point of the converging region of the channel exit, where the flow velocity magnitude through the channel with the above-mentioned point varied between the maximum range of 0.75 m/s and 1.5 m/s, while remaining the same in vertical and horizontal channels, i.e., the velocity magnitude remained at a minimum between the range of 0.05 and 0.75 m/s. Thus, electrolyte flow velocity contours visualize the smooth and uniform flow at the channel mid-plane for the highest flow rate of 150 mL/min.

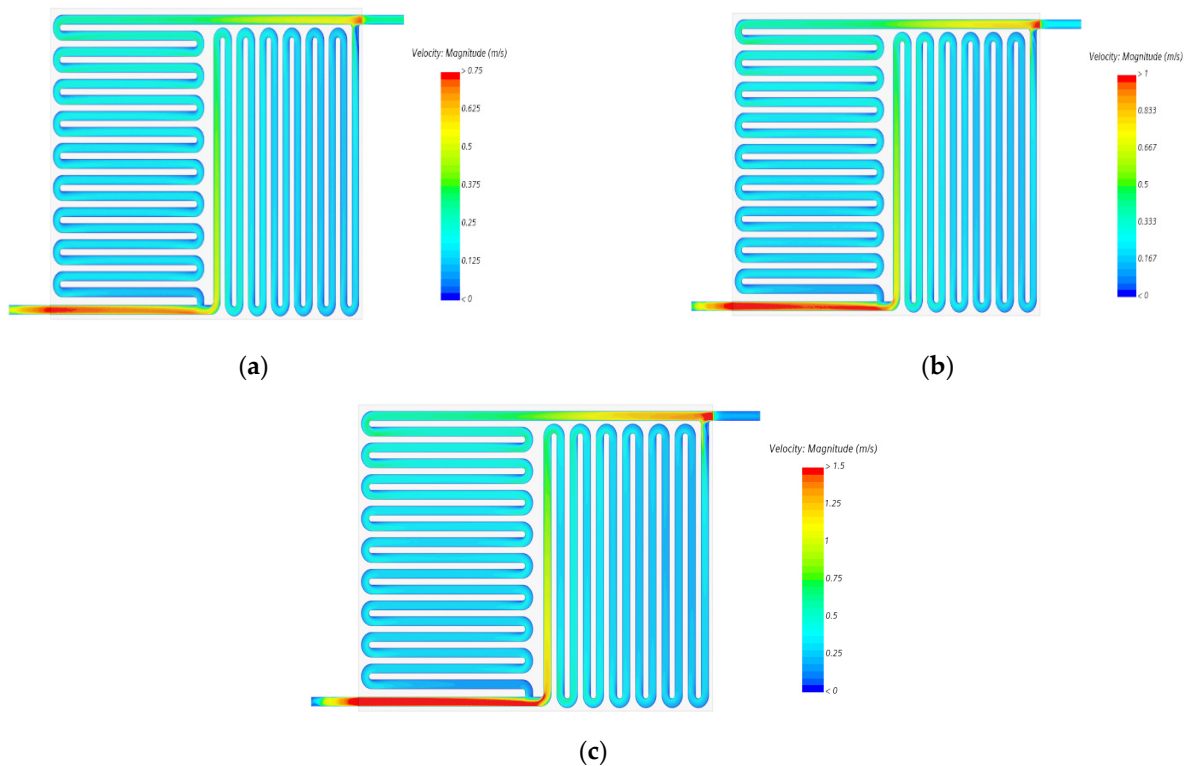


**Figure 14.** (a–c) Velocity magnitude at the mid-plane of Model D of the CSSFF channel for a flow rate of 150 mL/min.

Similar observations were made for three different cases, maintaining a constant maximum flow rate of 150 mL/min. We identified that the velocity magnitude pattern at the electrode mid-plane remained almost the same, but we found a higher velocity magnitude at the top portion of the felt region for the 70% compression ratio case, reaching up to 0.012 m/s, as shown in Figure 15c. However, for 50% and 60% CRs, the velocity magnitude through the electrode felt mid-plane exhibited a better flow distribution and maximum uniformity index of 0.827 and 0.820 for 50% and 60% CRs, respectively, as shown in Figure 15a,b.

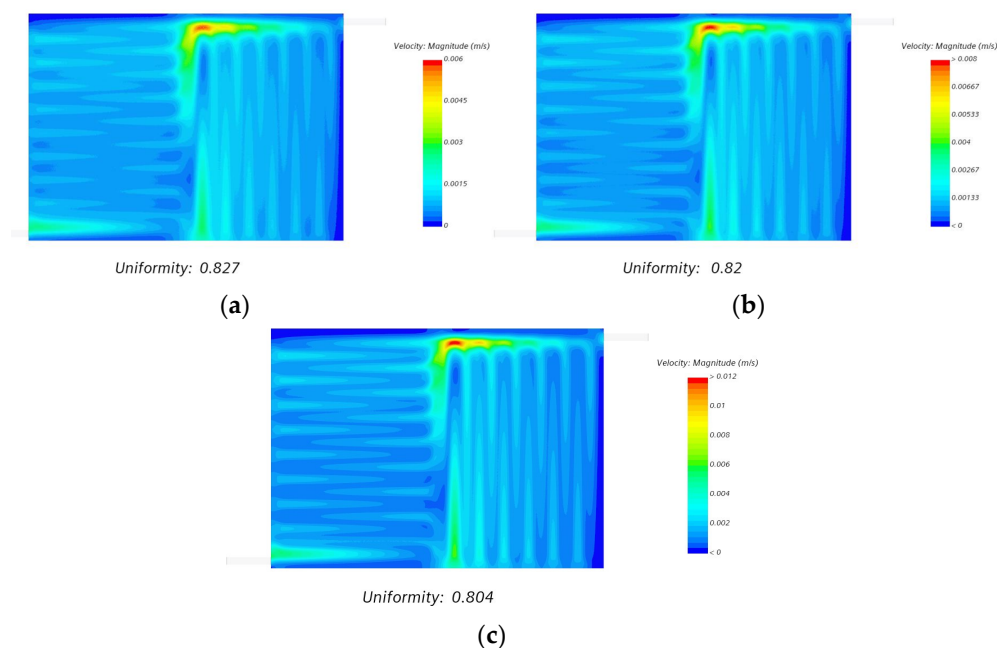


**Figure 15.** Predicted velocity magnitude at an electrode mid-plane for Model D of CSSFF with an electrode intrusion for a flow rate of 150 mL/min at CRs: (a) 50%; (b) 60; (c) 70%.

The minimum torque applied, equivalent to CR 50%, was required to hold the two halves of the cell tightly and uniformly to form the stack assembly, and also to prevent any leakages of the circulating electrolyte pumped from the external reservoir. To further study the electrode channel intrusion behavior on cell pressure drop, we considered two more CR values: 60% and 70%.

Table 5 presents a good understanding of the flow uniformity index, which is a predominant function of the compression ratio (CR), i.e., an increase in the CR value will gradually decrease the uniformity of flow distribution over an active cell area. This parametric variation, which was graphically projected and visualized, is depicted in Figure 16.

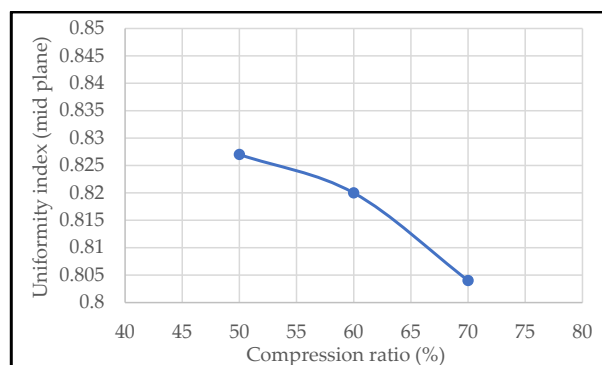


**Figure 16.** Uniformity index for Model D of CSSFF with an electrode intrusion at CRs of 50%, 60%, and 70% for a flow rate of 150 mL/min.

**Table 5.** Uniformity index values for different compression ratios.

Compression Ratio Percentage	Uniformity Index (Felt Mid)	Uniformity Index (Felt Volume)
50	0.827	0.768
60	0.820	0.749
70	0.804	0.721

The predicted simulation of volumetric flow distribution for each case visualized similar patterns to those depicted in Figure 17a–c, which show maximum volumetric flow magnitudes at the topmost portion of the mid-cell region and the bottom portion along the same line downward in the space between the vertical and horizontal channels, as well as at the channel exit region. These regions yielded the highest electrolyte concentration; however, the values shown in Table 5 suggest that the uniform volumetric flow distribution across an active cell area is a function of the compression ratio.

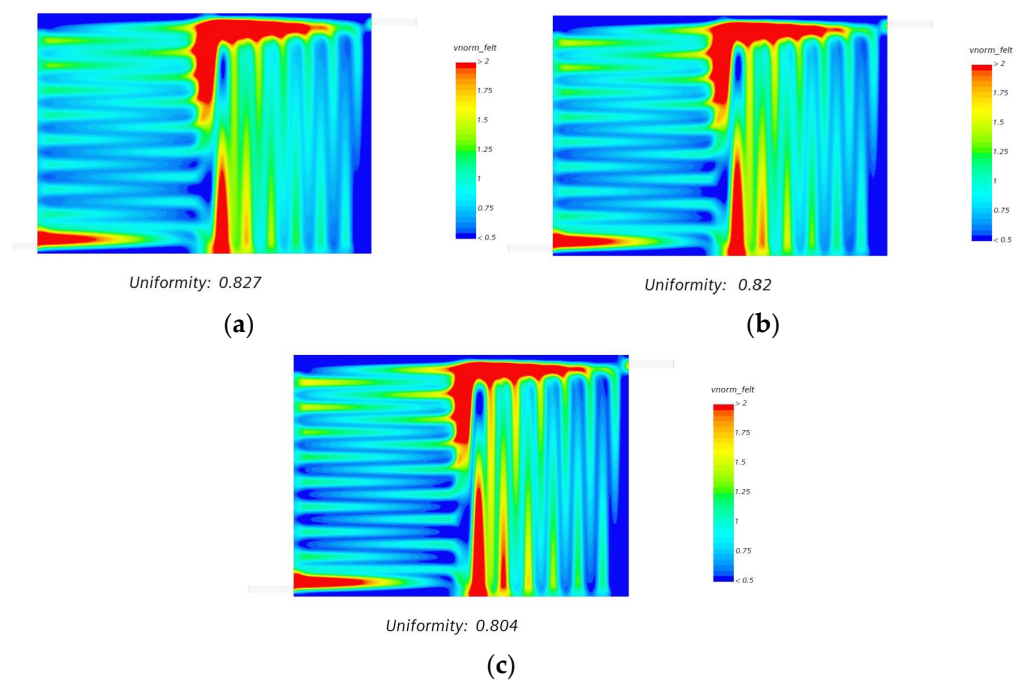


**Figure 17.** Predicted volumetric flow distribution at an electrode mid-plane for Model D of CSSFF with an electrode intrusion for a flow rate of 150mL/min at CRs: (a) 50%; (b) 60%; and (c) 70%.

### 6. Conclusions

An extensive study was conducted on the effect of flow hydrodynamics on a single and cross-split serpentine flow field for different geometrical configurations, i.e., channel-to-rib width ratios, over an active cell area of 131 cm<sup>2</sup>. The parameters measured experimentally, such as cell pressure drop ( $\Delta p$ ) through channels and with the presence of electrodes, were numerically validated using a CFD tool. The electrode felt channel intrusion behavior for both the flow fields, i.e., SCSFF and CSSFF at different CRs for various flow rates, was also numerically analyzed for flow velocity magnitude and flow distribution characteristics.

The following conclusions can be drawn from this study:

- A single-channel serpentine flow field (SCSFF) resulted in the highest pressure drop order of 31,815.35 Pa compared with a modified version of the cross-split serpentine flow field of Model D with 6941.12 Pa at CR 60% for a flow rate of 150 mL/min across an active cell area of 131 cm<sup>2</sup>.
- The compression ratio (CR) was found to be a strong function of electrode felt channel intrusion, which resulted in a reduced effective hydraulic diameter of the channel, which, in turn, reduced the effective flow area, causing an increased mean flow velocity.

- We also noticed that a reduced effective flow area would significantly increase the pressure drop,  $\Delta p$ , which was demonstrated by the simulation results at compression ratios of 50%, 60%, and 70% for a maximum flow rate of 150 mL/min, as depicted in Figures 12 and 13.
- We observed that skin friction is a function of the Reynolds number and gradually increased due to a reduction in the effective hydraulic diameter, which meant the flow velocity had increased.
- We also observed that even with an increase in the volumetric flow uniformity index of more than 80%, the flow velocity distribution over electrode felt was relatively uniform at different compression ratios, as shown in Figure 15.
- We also noticed that the influence of an intrusion effect was marginal on the flow distribution and uniformity throughout the electrode felt region.
- The CSSFF design was found to be the better choice over SCSFF in terms of volumetric flow uniformity through electrode mid and end planes, and might also reduce the mass transport polarization behavior, establishing an ideal ionic activity rate.
- In this study, Model D, a modified version of CSSFF, was found to be an optimal design suitable for the defined active cell area of 131 cm<sup>2</sup>, at different CRs, operating at a maximum flow rate of 150 mL/min.

**Author Contributions:** Conceptualization, R.B.K.; Formal analysis, R.B.K.; Methodology, R.B.K.; Investigation and software, R.B.K., A.D. and B.C.; Validation, R.B.K. and A.D.; Writing-original draft preparation, R.B.K.; Writing-review and editing, B.C.; Supervision, S.G.S. All authors have read and agreed to the published version of the manuscript.

**Funding:** This research received no external funding.

**Data Availability Statement:** Not applicable.

**Acknowledgments:** The facilities to conduct experiment was provided by Jyothy Institute of Technology, Fluid mechanics laboratory and relevant materials provided by Redox Flow Cell laboratory from CIIRC, Bengaluru, Karnataka, India.

**Conflicts of Interest:** The authors declare no conflict of interest.

## References

1. Yang, Z.; Liu, J.; Baskaran, S.; Imhoff, C.H. Enabling renewable energy and future grid—With advanced electricity storage. *Energy Storage Technol.* **2010**, *62*, 14–23. [CrossRef]
2. Dunn, B.; Kamath, H.; Tarascon, J.M. Electrical energy storage for the grid: A battery of choices. *Science* **2011**, *334*, 928–935. [CrossRef] [PubMed]
3. Yang, Z.; Zhang, J.; Kintner-Meyer, M.C.W.; Lu, X.; Choi, D.; Lemmon, J.P.; Liu, J. Electrochemical Energy Storage for Green Grid. *Chem. Rev. ACS Publ.* **2011**, *111*, 3577–3613. [CrossRef] [PubMed]
4. Emerging Technology News Customized Energy Solutions India Pvt. Ltd. Available online: <https://etn.news/energy-storage/classification-of-energy-storage-technologies-an-overview> (accessed on 21 September 2020).
5. Hossain, E.; Faruque, H.M.R.; Sunny, M.S.H.; Mohammad, N.; Nawar, N. A Comprehensive Review on Energy Storage Systems: Types, Comparison, Current Scenario, Applications, Barriers, and Potential Solutions, Policies, and Future Prospects. *Energies* **2020**, *13*, 3651. [CrossRef]
6. Skyllas-Kazacos, M.; Chakrabarti, M.H.; Hajimolana, S.A.; Mjalli, F.S.; Saleem, M. Progress in Flow Battery Research and Development. *J. Electrochem. Soc.* **2011**, *158*, 55–79. [CrossRef]
7. Ponce-de-León, C.; Frías-Ferrer, A.; González-García, J.; Szánto, D.A.; Walsh, F.C. Redox flow cells for energy conversion. *J. Power Sources* **2006**, *160*, 716–732. [CrossRef]
8. Kumar, M.N.; Kumar, S.M.; Vijayakumar, G.C.; Kadirgama, K.; Samykano, M.; Venkatesh, K.; Murlidhara, H.B. Effect of Flow Field Geometry on Hydrodynamics of Flow in Redox Flow Battery. *Energy Eng. Tech. Sci. Press* **2021**, *119*, 201–217.
9. Arenas, L.F.; de León, C.P.; Walsh, F.C. Redox flow batteries for energy storage: Their promise, achievements and challenges. *Curr. Opin. Electrochem.* **2019**, *16*, 117–126. [CrossRef]
10. Di Noto, V.; Vezzu, K.; Crivellaro, G.; Pagot, G.; Sun, C.; Meda, L.; Zawodzinski, T.A. A general electrochemical formalism for vanadium redox flow batteries. *Electro. Chim. Acta* **2022**, *408*, 139937. [CrossRef]
11. Zhang, H.; Chen, N.; Luo, X. Investigations on physicochemical properties and electrochemical performance of graphite felt and carbon felt for iron-chromium redox flow battery. *Int. J. Energy Res.* **2020**, *44*, 3839–3853. [CrossRef]

12. Zhang, H.; Sun, C. Cost-effective iron-based aqueous redox flow batteries for large-scale energy storage application: A review. *J. Power Sources* **2021**, *493*, 229445. [[CrossRef](#)]
13. Weber, A.Z.; Mench, M.M.; Meyers, J.P.; Ross, P.N.; Gostick, J.T.; Liu, Q. Redox flow batteries: A review. *J. Appl. Electrochem.* **2011**, *41*, 1137–1164.
14. Gundlapalli, R.; Jayanti, S. Effect of channel dimensions of serpentine flow fields on the performance of a vanadium redox flow battery. *J. Energy Storage* **2019**, *23*, 148–158. [[CrossRef](#)]
15. Lisboa, K.M.; Marschewski, J.; Ebejer, N.; Ruch, P.; Cotta, R.M.; Michel, B.; Poulikakos, D. Mass transport enhancement in redox flow batteries with corrugated fluidic networks. *J. Power Sources* **2017**, *359*, 322–331. [[CrossRef](#)]
16. Arenas-Martínez, L.F.; Ponce de León, C.; Walsh, F.C. Engineering aspects of the design, construction and performance of modular redox flow batteries for energy storage. *J. Energy Storage* **2017**, *11*, 119–153. [[CrossRef](#)]
17. Brown, L.D.; Tobias, P.; Neville, T.; Jervis, R.; Mason, T.J.; Shearing, P.R.; Brett, D.J.L. The effect of felt compression on the performance and pressure drop of all-vanadium redox flow batteries. *J. Energy Storage* **2016**, *8*, 91–98. [[CrossRef](#)]
18. Chang, T.C.; Zhang, J.P.; Fuh, Y.K. Electrical, mechanical and morphological properties of compressed carbon felt electrodes in vanadium redox flow battery. *J. Power Sources* **2014**, *245*, 66–75. [[CrossRef](#)]
19. Jyothi Latha, T.; Jayanti, S. Ex-situ experimental studies of serpentine flow fields for redox flow battery applications. *J. Power Sources* **2014**, *248*, 140–146. [[CrossRef](#)]
20. Darling, R.M.; Perry, M.L. The influence of electrode and channel configurations on flow battery performance. *J. Electro. Chem. Soc.* **2014**, *161*, A1381–A1387. [[CrossRef](#)]
21. Xu, Q.; Zhao, T.S.; Zhang, C. Performance of a vanadium redox flow battery with and without flow fields. *Electro. Chem. Acta* **2014**, *142*, 61–67. [[CrossRef](#)]
22. Aaron, D.S.; Liub, Q.; Tanga, Z.; Grimb, G.M.; Papandrewa, A.B.; Turhanb, A.; Zawodzinska, T.A.; Mench, M.M. Dramatic performance gains in vanadium redox flow batteries through modified cell architecture. *J. Power Sources* **2012**, *206*, 450–453. [[CrossRef](#)]
23. Ke, X.; Prahl, J.M.; Alexander, D.; Savinell, R.F. Redox flow batteries with serpentine flow fields: Distributions of electrolyte flow reactant penetration into the porous carbon electrodes and effects on performance. *J. Power Sources* **2018**, *384*, 295–302. [[CrossRef](#)]
24. Gerhardt, M.R.; Wong, A.A.; Aziz, M.J. The Effect of Interdigitated Channel and Land Dimensions on Flow Cell Performance. *J. Electrochem. Soc.* **2018**, *165*, A2625–A2643. [[CrossRef](#)]
25. Kumar, S.; Jayanti, S. Effect of electrode intrusion on pressure drop and electrochemical performance of an all-vanadium redox flow battery. *J. Power Sources* **2017**, *360*, 548–558. [[CrossRef](#)]
26. Kumar, S.; Jayanti, S. Effect of flow field on the performance of an all-vanadium redox flow battery. *J. Power Sources* **2016**, *307*, 782–787. [[CrossRef](#)]
27. Maharudrayya, S.; Jayanti, S. Flow distribution and pressure drop in parallel-channel configurations of planar fuel cells. *J. Power Sources* **2004**, *144*, 94–106. [[CrossRef](#)]
28. Moro, F.; Trovo, A.; Bortolin, S.; Del Col, D.; Guarnieri, M. An alternative low-loss stack topology for vanadium redox flow battery: Comparative assessment. *J. Power Sources* **2017**, *340*, 229–241. [[CrossRef](#)]
29. Zheng, Q.; Xing, F.; Li, X.; Ning, G.; Zhang, H. Flow field design and optimization based on the mass transport polarization regulation in a flow-through type vanadium flow battery. *J. Power Sources* **2016**, *324*, 402–411. [[CrossRef](#)]
30. Zhou, X.L.; Zhao, T.S.; Zeng, Y.K.; An, L.; Wei, L. A highly permeable and enhanced surface area carbon-cloth electrode for vanadium redox flow batteries. *J. Power Sources* **2016**, *329*, 247–254. [[CrossRef](#)]
31. Xu, Q.; Zhao, T.S.; Leung, P.K. Numerical investigations of flow field designs for vanadium redox flow batteries. *Appl. Energy* **2013**, *105*, 47–56. [[CrossRef](#)]
32. You, X.; Ye, Q.; Cheng, P. Scale-up of high power density redox flow batteries by introducing interdigitated flow fields. *Int. Commun. Heat. Mass. Transf.* **2016**, *75*, 7–12. [[CrossRef](#)]
33. Prasad, K.B.S.; Jayanti, S. Effect of channel-to-channel cross flow on local flooding in serpentine flow fields. *J. Power Sources* **2008**, *180*, 227–231. [[CrossRef](#)]
34. Xu, C.; Zhao, T.S. A new flow field design for polymer electrolyte-based fuel cells. *Electro. Chem. Commun.* **2007**, *9*, 497–503. [[CrossRef](#)]
35. Suresh, P.V.; Jayanti, S.; Deshpande, A.P.; Haridoss, P. An improved serpentine flow field with enhanced cross-flow for fuel cell applications. *Int. J. Hydrogen Energy* **2011**, *36*, 6067–6072. [[CrossRef](#)]
36. Gundlapalli, R.; Jayanti, S. Performance characteristics of several variants of interdigitated flow fields for flow battery applications. *J. Power Sources* **2020**, *467*, 228225. [[CrossRef](#)]
37. Rakesh, B.K.; Gowreesh, S.S.; Deshpande, A. Numerical investigation of hydrodynamics in a flow field and porous substrate configuration for redox flow battery application. *J. Mines Met. Fuels* **2023**, *in press*.
38. Prumbohm, E.; Becker, M.; Fleischlen, S.; Wehinger, G.D.; Turek, T. Flow field designs developed by comprehensive CFD model decrease system costs of vanadium redox-flow batteries. *J. Flow Chem.* **2021**, *11*, 461–481. [[CrossRef](#)]
39. Jyothi Latha, T.; Jayanti, S. Hydrodynamic analysis of flow fields for redox flow battery applications. *J. Appl. Electro. Chem.* **2014**, *44*, 995–1006. [[CrossRef](#)]

40. Knudsen, E.; Albertus, P.; Cho, K.T.; Weber, A.Z.; Kojic, A. Flow simulation and analysis of high-power flow batteries. *J. Power Sources* **2015**, *299*, 617–628. [[CrossRef](#)]
41. Tamayol, A.; McGregor, F.; Bahrami, M. Single phase through-plane permeability of carbon paper gas diffusion layers. *J. Power Sources* **2012**, *204*, 94–99. [[CrossRef](#)]

**Disclaimer/Publisher’s Note:** The statements, opinions and data contained in all publications are solely those of the individual author(s) and contributor(s) and not of MDPI and/or the editor(s). MDPI and/or the editor(s) disclaim responsibility for any injury to people or property resulting from any ideas, methods, instructions or products referred to in the content.